Validation of Floating Node Method Using Three-Point Bend Doubler Under Quasi-Static Loading

Alex S. Selvarathinam[1]
Lockheed Martin Aeronautics Company, Fort Worth, TX, 76101.

Nelson V. De Carvalho[2] and Banavara R. Seshadri[3]
National Institute of Aerospace, resident at Durability and Damage Tolerance, and Reliability Branch, NASA Langley Research Center, Hampton, VA, 23681.

Vivian Johnson[4]
Lockheed Martin Aeronautics Company, Marietta, GA, 30063.

William M. Johnston[5], Wade C. Jackson[6], Cheryl A. Rose[7], Thomas K. O'Brien[8]
NASA Langley Research Center, Hampton, VA, 23681.

The NASA Advanced Composite Project (ACP), an industry/government/university partnership, has embarked upon the task of developing technology that can aid in reducing the time line for structural certification of aircraft composite parts using a combination of technologies, one of which is high fidelity damage progression computational methods. Phase II of this project included a task for validating an approach based on the Floating Node Method combined with Directional Cohesive Elements (FNM-DCZE). This paper discusses predicted damage onset and growth in a three-point bend doubler specimen compared to experimental results. Sensitivity of the simulations to mesh refinement as well as key material properties and thermal effects are studied and reported. Overall, qualitative results suggest the main aspects of the damage progression have been captured, with the simulated damage morphology and sequence of events resembling closely what was observed experimentally. Quantitatively, the first load-peak is predicted. However, the re-loading observed in the experiments, after the first load peak, is not captured numerically, suggesting further investigation may be worth pursuing.

I. Nomenclature

ACP	=	Advanced Composites Project
AE	=	Acoustic Emission
BBA	=	Building Block Approach
BVID	=	Barely Visible Impact Damage
CAT	=	Computer Aided Tomography
CZM	=	Cohesive Zone Method

[1] Aeronautical Engineer Senior Staff, AIAA Associate Fellow
[2] Senior Research Engineer, Member AIAA
[3] Associate Principal Engineer
[4] Aeronautical Engineer Staff
[5] Senior Research Engineer
[6] Senior Research Aerospace Engineer
[7] Senior Research Aerospace Engineer, Member AIAA
[8] Senior Research Aerospace Engineer

DCZE = Directional Cohesive Zone Element
DIC = Digital Image Correlation
FNM = Floating Node Method
LVDT = Linear Variable Differential Transformer
PDFA = Progressive Damage Failure Analysis
t_s = Skin Thickness
t_d = Flange Thickness
UT = Ultrasonic Technique

II. Introduction

Composite structural aircraft parts are certified using analysis (closed form/semi-empirical) supported by extensive testing guided by the Building Block Approach (BBA) framework [1]. This process is typically time consuming and expensive. The NASA Advanced Composites Project (ACP) seeks to develop and transition technology that will enable reduction in the timeline required for development and certification of new aircraft structure that use advanced composite materials. High-fidelity analysis methods that can reliably predict the onset of damage and damage progression in composite materials can contribute to this goal by replacing some of the testing requirements in the current largely empirical BBA used for the design and certification of aircraft structure. Additionally, these analysis methods offer the potential for the development of more efficient structural concepts by enabling the exploration of the large design space of laminated composites, which is not possible with the current approach for structural design and substantiation. To achieve this goal requires the detailed and quantitative evaluation and development of progressive damage failure analysis (PDFA) methods for prediction of fatigue life and residual strength of composite structures, as well as a durability and damage tolerance database on composite sub-elements, elements, and structural subcomponents for validation of progressive damage analysis methods.

Failure of stiffened structures by debonding of the stiffener in the post-buckled regime is a critical failure mode of both pristine and impact damaged stiffened composite structures, and was selected as one of the challenge problems for residual strength and life prediction to be addressed by the ACP.

A key objective of the NASA ACP effort is to evaluate the capability of the selected high fidelity PDFA methods to predict strength and life of an impacted complex aircraft structural part, such as a cocured multi-stringer panel [2]. The damage mechanisms are complex, involving both damage within plies (intralaminar) and delamination/disbond between plies (interlaminar). The risk posed by these complex damage mechanisms acting independently and/or interactively are currently managed within the BBA framework, which involves extensive testing. In order to be used in certification, PDFA must accurately capture these damage mechanisms and predict failure within prescribed accuracy. An important step in this process is to first validate the PDFA damage model with a simple experiment that captures the physics of the damage mechanism before trying to predict similar damage in a more complex structure. To this effect, the "three-point bend doubler" specimen was designed and included as part of the validation building block. It is a simple configuration that includes many of the complicating factors of interacting matrix cracks and delaminations, which is typical of skin-stiffener separation in complex components.

In the NASA ACP Phase II effort, one of the tasks is to validate the interlaminar and intralaminar damage observed in a three-point doubler with the Directional Cohesive Zone Element (DCZE) [3] as implemented within a Floating Node Method (FNM) framework. The FNM enables the discrete representation of a network of cracks by splitting a finite element into integrable sub-elements through the use of floating nodes [4]. The paths of the cracks are not necessarily known a priori. Matrix crack and delamination onset and delamination migration are captured using Directional Cohesive Zone Element (DCZE) approach, based on Cohesive Zone Method (CZM) [5]. In this study, the FNM method is implemented as an Abaqus/Standard® user defined element. This paper discusses the preliminary results of this task.

III. Experimental Configuration

The experimental setup, including load, displacement, and strain measurement devices; non-destructive inspection techniques; and specimen lay-up information are discussed in this section.

The three-point bend doubler specimen and test set-up are shown in Figure 1. The specimen consists of an IM7/8552 plain-weave fabric doubler co-cured with an IM7/8552 unidirectional tape skin laminate. The specimens are nominally 304.8-mm long, 25.4-mm wide, and the doubler is nominally 101.6-mm long. The stacking sequences for the skin and for the flange are $[+45/-45/0/90/45/-45]_S$ and $[+45/-45/0/+45/+45/0/-45/+45/+45/-45/0/45]_T$ respectively, where the 0-degree direction is parallel to the flange edge. The first ply in the flange stacking sequence is adjacent to the skin.

The specimen was supported on rollers and the load was applied at the center of the specimen through a central roller. The support rollers and the loading nose have a 50.8-mm diameter, and a 12.7-mm diameter, respectively. The specimens were loaded under displacement control at a rate of 1.27 mm/min. A linear variable differential transformer (LVDT) was placed beneath the center of the flange section and at the specimen midlength as shown in Figure 1 to monitor center-point out-of-plane displacements. Strains near the flange termination were monitored with back-to-back strain gages on the skin section, at the specimen centerline, and 12.7 mm from the flange termination location. Three-dimensional digital image correlation (DIC) systems were used on the specimen front and back edges to provide full field 3-D displacement data throughout the specimen loading. The DIC systems were also used to monitor the development and propagation of front and back surface transverse matrix cracks and delaminations. Acoustic emission (AE) sensors placed at the ends of the specimen, and the DIC data were used to provide an indication of damage initiation and propagation during the test.

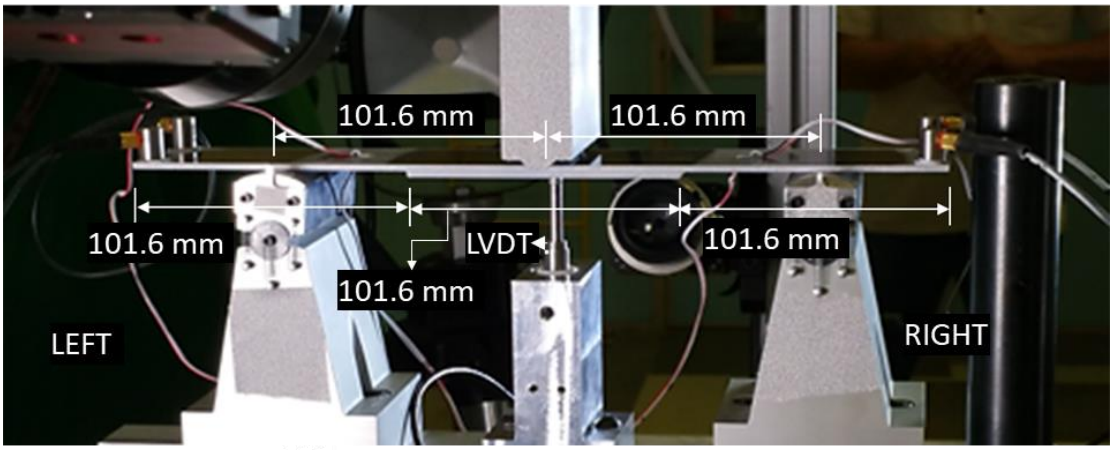

Figure 1. Three-Point Bend Doubler Specimen and loading apparatus.

The nominal thicknesses of skin (t_s), flange (t_d), and specimen width are shown in Figure 2.

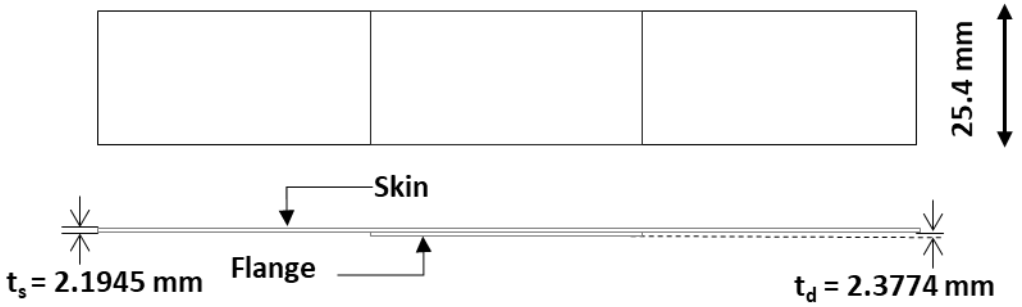

Figure 2. Geometry of Three-point Bend Doubler Specimen

IV. Finite Element Model and Material Data

This section presents an overview of the methodology, finite element model, and material properties employed in this study. The methodology was implemented in Abaqus/Standard® as a user defined element subroutine.

A. FNM-DCZE Methodology

The extended interface element consists of a 3D 48-node element, composed of 16 real nodes which have pre-assigned positions (Figure 3a), and 32 floating nodes, as shown in Figure 3b. The 16 real nodes define the sub-elements above and below the interface. The 32 floating nodes facilitate further splitting of the two sub-elements independently. The floating nodes are part of the element connectivity. However, if the sub-elements do not split, the floating nodes can be condensed out of the system of equations. Since the connectivity of the floating nodes is defined a priori, when activated, they naturally enforce crack path continuity. For example, an edge will be split by a unique pair of floating nodes shared by all the elements sharing that edge, as defined by their connectivity list. The element, as proposed, can be used to represent matrix cracks of any in-plane orientation. As matrix cracks nucleate as shown in Figure 3b, the interface element may also be split using floating nodes, and interface elements are assigned as required to model the subsequent opening of the newly generated splits.

As depicted in Figure 3b, the matrix cracks are assumed to be normal to the interfacial plane to facilitate integration of partitioned elements. However, matrix cracks will only be normal to the interacial plane if forming under predominantly tensile loads; otherwise, their angle may vary. To mitigate the effect of this approximation, the present study uses two corrections. The first consists of determining the tractions in a rotated coordinate system, following References [7] and [8]. In addition, since the matrix cracks are free to follow a mode I path as they propagate through-thickness, it is also considered that the shear component determined along direction 1 in Figure 3c, if not zero, does not contribute to the mode-mixity. The DCZE, which is a variation of CZM, enhances the CZM approach with the ability of predicting delamination growth away from an interface between two plies. Since the delamination can potentially grow into either of the two plies bounding the interface (i.e., migrate), DCZE uses crack growth direction information and stress state [6] to determine the necessary conditions for migration, and its direction, treating the formation of matrix cracks that may lead to migration as a continuation of the delamination rather than a separate event. Additional details regarding the FNM-DCZE methodology are provided in Reference [9].

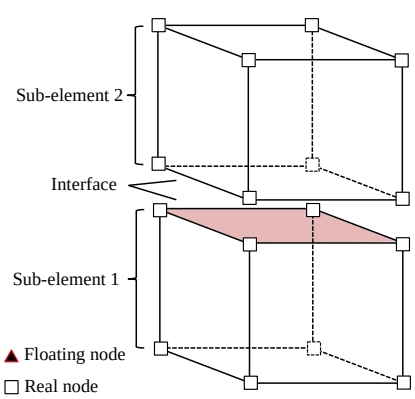

(a) Pristine extended interface element with sub-elements above and below an interface

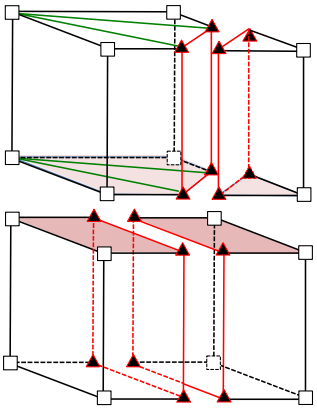

(b) Element representing matrix cracks

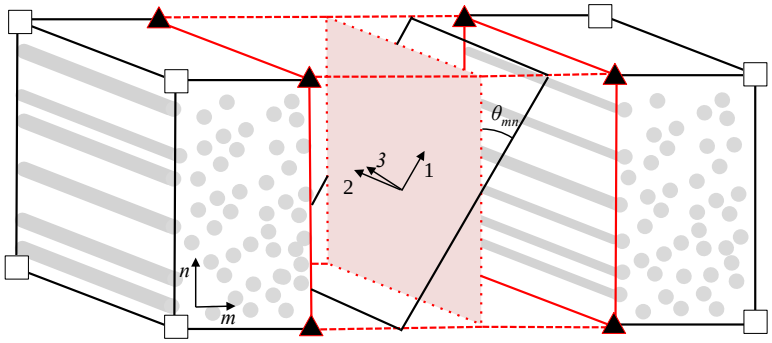

(c) Matrix crack through thickness approximation

Figure 3. Extended Interface Element. Distances between Sub-Elements and Partitions are Exaggerated for Illustration Purposes.

B. Finite Element Model

A 1/5th width-scaled model (strip model) was employed in this study (Figure 4). The scaled model is used to perform sensitivity studies, investigate mesh objectivity, and identify the requirements that will guide full scale models. The model is composed of a global region, modeled using abaqus native continuum shell elements and a local refined mesh region near one flange termination defined by the lengths L_1 and L_2, as shown in Figure 4. In this local region FNM elements were used. The in-plane dimensions of the local region are given in Figure 4. Through-the-thickness, the local region encompassed half of the first fabric ply and the first three skin layers. The discretization through-the-thickness was equal to or less than 1 floating node element per ply. The in-plane mesh sizes and lengths used in the FNM region are shown in Table 1. The FNM region was connected to the global model via tie constraints. The model was loaded via rigid cylindrical indentors with the same radius as used in the experiments (see previous section).

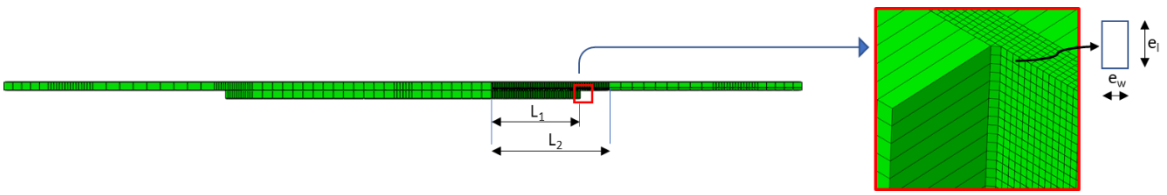

Figure 4. 1/5th Wide Scaled Three-Point Bend Finite Element Model.

Table 1. Mesh Refinement Parameters

Model	Width (mm)	L_1 (mm)	L_2 (mm)	e_w (mm)	e_l (mm)
MS1	5	25.4	33.7	0.14	0.169
MS2	5	25.4	33.7	0.25	0.25
MS3	5	25.4	33.7	0.3175	0.5
MS4	5	25.4	46.4	0.25	0.25

C. Material Properties

The material properties employed for the three-point bend model are shown in Table 2. E_{11}, E_{22}, and E_{33} are the Young's moduli in the 11, 22, and 33 direction respectively; ν_{12}, ν_{13}, and ν_{23} are the Poisson's ratio; G_{12}, G_{13}, and G_{23} are the shear moduli in the 12, 13, and 23 planes respectively; G_{IC}, G_{IIC}, and G_{IIIC} are the mode I, II, and III critical strain energy release rates, respectively, associated with damage onset; G_{IR}, G_{IIR}, and G_{IIIR} are the mode I, II, and III critical strain energy release rates, respectively, associated with steady state delamination growth. Transverse isotropy was assumed in the 2-3 plane. η is the Benzeggagh and Kenane (BK) exponent [10].

Table 2. Tape/Fabric Material Properties

IM7/8552 Elastic Tape Properties								
E_{11} (GPa)	**E_{22} (GPa)**	**E_{33} (GPa)**	**ν_{12}**	**ν_{13}**	**ν_{23}**	**G_{12} (GPa)**	**G_{13} (GPa)**	**G_{23} (GPa)**
146.7	8.7	8.7	0.32	0.32	0.45	5.2	5.2	3
IM7/8552 Tape/Tape Interface Strength and Fracture Toughness Properties								
G_{IC} (N.mm^{-1})	**G_{IIC} (N.mm^{-1})**	**G_{IIIC} (N.mm^{-1})**	**η**	**K_n (MPa/mm)**	**K_s (MPa/mm)**	**Y_T (MPa)**	**Y_S (MPa)**	
0.24	0.739	0.739	2.17	50000	50000	80/89	140/156	
IM7/8552 Elastic Fabric Properties								
E_{11} (GPa)	**E_{22} (GPa)**	**E_{33} (GPa)**	**ν_{12}**	**ν_{13}**	**ν_{23}**	**G_{12} (GPa)**	**G_{13} (GPa)**	**G_{23} (GPa)**
66	66	40	0.01	0.53	0.43	5.1	5.2	3.4
IM7/8552 Tape/Fabric Interface Strength and Fracture Toughness Properties – Damage Onset								
G_{IC} (N.mm^{-1})	**G_{IIC} (N.mm^{-1})**	**G_{IIIC} (N.mm^{-1})**	**η**	**K_n (MPa/mm)**	**K_s (MPa/mm)**	**Y_T (MPa)**	**Y_S (MPa)**	
0.29	1.228	1.228	1.3	50000	50000	80	163	
IM7/8552 Tape/Fabric Interface Strength and Fracture Toughness Properties – Damage Propagation								
G_{IR} (N.mm^{-1})	**G_{IIR} (N.mm^{-1})**	**G_{IIIR} (N.mm^{-1})**	**η**	**K_n (MPa/mm)**	**K_s (MPa/mm)**	**Y_T (MPa)**	**Y_S (MPa)**	
0.581	1.339	1.339	1	50000	50000	89	135	

.

The interface properties K_n and K_s are the normal and shear penalty stiffness, respectively, while Y_T and Y_S are the normal and shear interface strengths, respectively. These interface properties are derived from the measured properties as discussed in Reference [11]. Y_T is assumed equal the in-plane transverse tensile strength, measured using a uniaxial tensile specimen [12] and Y_S is determined such that the fracture process zone length is the same for Mode I and II. The nominal thicknesses of a tape and a fabric ply are 0.183 mm and 0.198 mm, respectively.

V. Results and Discussion

Preliminary results for the three-point bend experiments and analysis using FNM are discussed next. A typical specimen response and overall discussion of the experimental observations is presented first. Next, the results of mesh

refinement study are presented, followed by comparison of the model predictions with experiment. This section concludes with a study of the sensitivity of the simulations to selected parameters.

A. Typical Response

Load versus displacement curves for five specimens are provided in Figure 5. For the specimens tested incrementally (Specimens IL), the curves shown are a compilation of data obtained from all the incremental tests for that specimen.

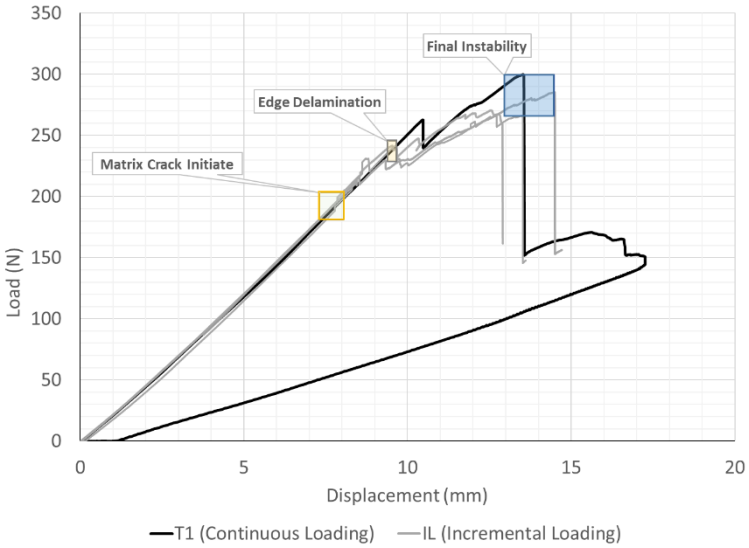

Figure 5. Load versus Displacement Response for all Specimens Tested.

During the initial loading, the specimen response exhibits some stiffening resulting from a decrease in moment arm due to the specimen rotation. During this phase of loading, testing was interrupted based on acoustic emission signals. The specimen was then examined by X-Ray/CT to identify the onset of matrix cracking. As such, onset of matrix cracking was defined as the first instance of matrix cracking visible by X-Ray/CT. For all tests, the scan resolution was 14 μm/voxel. Matrix cracking was observed to develop in the top +45° ply of the skin in all of the specimens, after loading to between 180 N and 200 N, as shown in Figure 5. On subsequent loading the response remained linear up to the point of a delamination developing between the skin and the flange on one flange edge. The development of the delamination was characterized by a load drop in the load versus displacement response and occurred at a load level between 228 and 245 N (box labeled "Edge Delamination" in Figure 5) for all specimens. Upon further loading of the specimen loaded straight to failure (specimen T1) the delamination continued to grow gradually on one flange edge, until reaching sufficient length that the propagation became unstable. In the remaining specimens, continued loading resulted in development of delamination on the other flange edge. Increasing the load led to further propagation of damage on both flange edges until damage growth on one flange edge dominated the response and the specimen failed. Specimen failure, for all specimens tested, occurred between 267 and 285 N. The side of the specimen on which the delamination developed first varied from specimen to specimen, and was possibly influenced by slight misalignment of the specimen in the load fixture.

Details of the damage development and the complexity of the damage are summarized in the X-Ray/CT images in Figure 6. The X-Ray/CT images are planes parallel to the top and bottom surfaces of the specimen, extracted at through-the-thickness locations of the flange/skin interface and ply interfaces. The sharp black lines are matrix cracks, and the grey-black areas are delaminations. Damage initiates close to the flange-skin intersection and is characterized by matrix cracking in the top +45° and -45° plies and delaminations at the flange/skin interface and at the 45°/-45° interface. The delaminations are not continuous across the specimen width on either interface, but rather the damage is a complex interaction of matrix cracks in the +45° ply and delaminations that alternate between the two interfaces through the matrix cracks in the +45° ply. Upon further loading, the cracks in both the +45° and -45° plies and the delaminations at the flange/skin interface and the 45/-45 interface continued to grow and extended further into the

specimen, away from the flange edge. This growth continued with further loading, and delaminations began to develop at the -45°/0° interface in the interior of the specimen. Further loading led to one or more cracks in the 45° ply apparently propagating across the specimen width, delaminations at the flange/skin and +45°/-45° interfaces linking up to form complete delaminations between the 45° cracks and the specimen edges, and finally delamination migration through cracks in the 0° down to the 0° /90° interface.

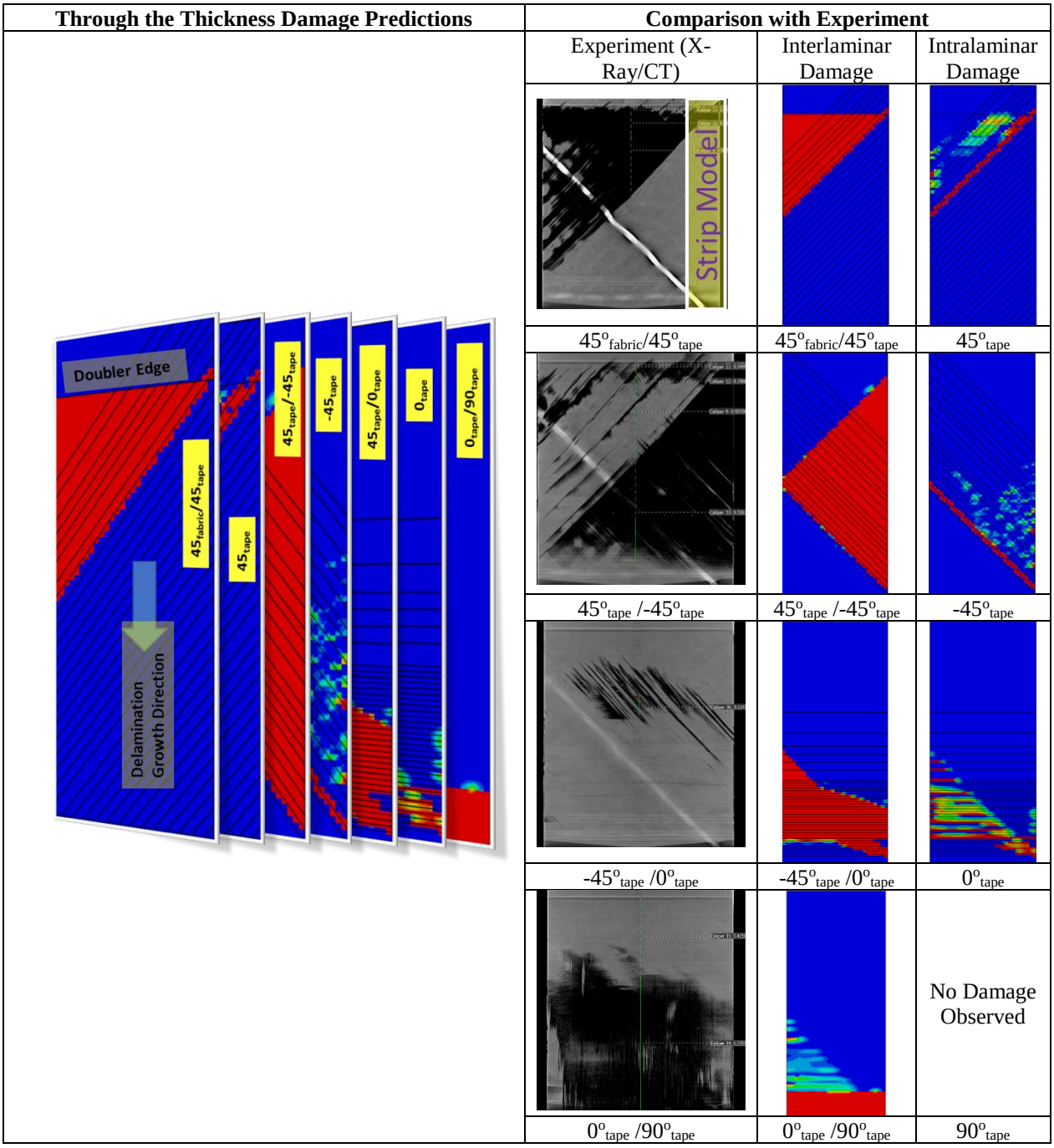

Figure 6. Interlaminar, Intralaminar Damage and Crack Migration Compared to Experiment.

B. Mesh-size study

The effect of mesh size (see Table 1) on the load-displacement simulation results is shown in Figure 7. For this analysis G_c related to damage onset was used. The variation in peak load is less than 4% for four different mesh refinements considered.

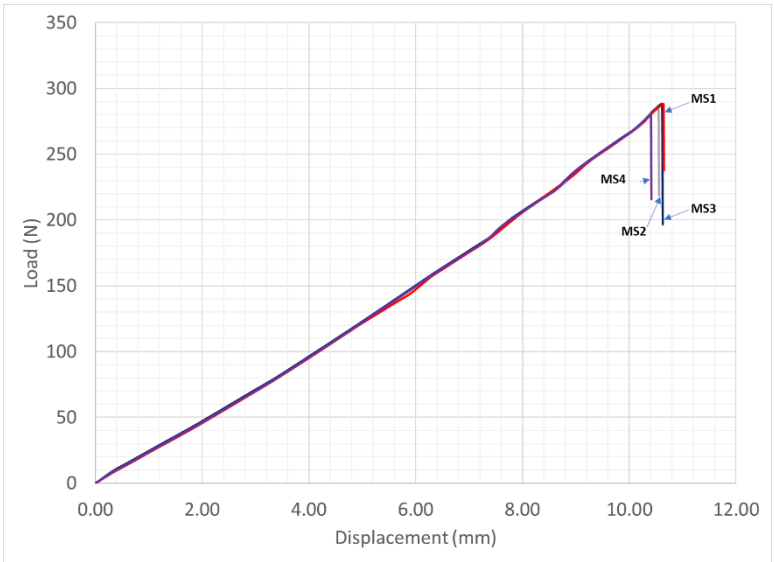

Figure 7. Sensitivity of Predicted Load versus Displacement Response to Mesh Size and Refinement.

C. Nominal results (G_c)

The predicted load versus displacement plot for Model MS1 (described in Table 1) for the scaled three-point bend specimen is compared with experimental results in Figure 8. For this analysis, the critical energy release rate related to damage onset, G_c, was used.

The slope of the analytical curve matches the test results (T1 and IL); however, the predicted peak stress is lower than the experiments. A possible reason for this is discussed in Subsection D.1 in relation to the damage progression energy release rate (G_R) and the transverse interfacial normal strength (Y_T). Note that test T1 was loaded continuously until a delamination length of 38.1 mm was observed on one of the sides, while the other tests (IL) were stopped intermittently to measure the damage using ultrasonic UT and X-ray/CT.

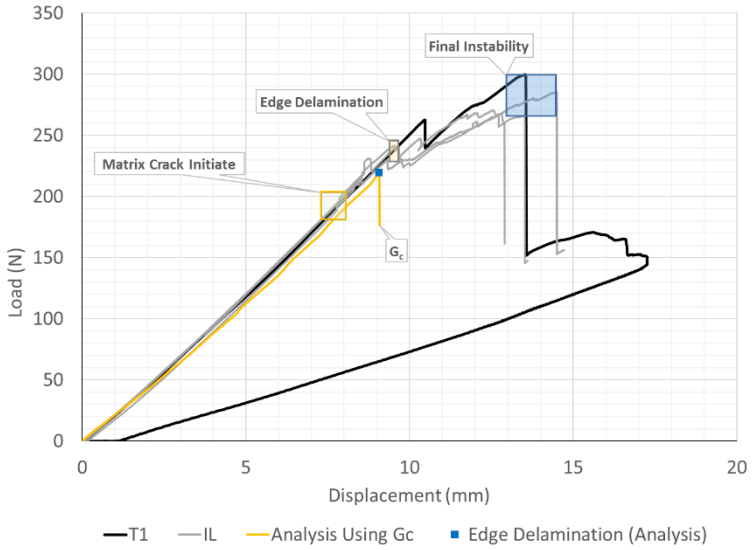

Figure 8. Predicted Load Displacement Response for Model MS1 using Initiation Energy Release Rate, G_c.

The damage morphology observed in model MS1, defined in Table 1, is compared to experimental results in Figure 6. In the X-Ray/CT, the black areas are regions of delaminations. These same delaminations are shown as red in the interlaminar damage plots on the right. Splits are displayed as black lines running along the fiber direction. These are inserted when the cohesive strength is exceeded anywhere along their length. These splits are closed initially and will turn red when they are open fully, representing at that point fully formed matrix cracks, as shown in the intralaminar damage plots.

Interlaminar damage was observed in the $45^o_{fabric}/45^o_{tape}$ interface, which subsequently migrated through the 45^o_{tape} ply as matrix cracks. These matrix cracks instigated further delamination in the $45^o_{tape}/-45^o_{tape}$ interface below. Subsequently, the delamination in the $45^o_{tape}/-45^o_{tape}$ interface migrated through the -45^o_{tape} ply. As the load increased, the matrix cracks in the -45^o_{tape} ply caused additional delamination in the $-45^o_{tape}/0^o_{tape}$ interface below, which subsequently resulted in matrix cracks in the 0^o_{tape} ply that led to delamination in the $0^o_{tape}/90^o_{tape}$ interface. The overall sequence of events seems to be captured well by the scaled model, as can be seen in Figure 6. The main discrepancy is the larger delamination in the $-45^o_{tape}/0^o_{tape}$ interface in the model before migration to the $0^o_{tape}/90^o_{tape}$ occurs.

D. Sensitivity Study

In this section the sensitivities of both the load-displacement curve and damage morphology to the critical energy release (G_c vs G_R) and interface strength (Y_T), cohesive law used (bi-linear vs tri-linear), and thermal residual stresses are investigated.

1. Damage onset (G_c), Damage progression (G_R) critical energy release rates and Transverse Interface Normal Strength (Y_T)

The critical energy release rate used in the analysis, G_c, is typically obtained from standardized tests, and is associated with the energy required to grow damage from a predefined flaw. However, as the delamination grows, depending on the mode-mixity and bounding plies, a marked increase in the energy required to grow a crack can be observed [13]. This may be due to several mechanisms, including fiber bridging, surface texture, etc. [14]. This steady state critical energy release rate is denoted as G_R.

A bi-linear cohesive law cannot capture the transition from G_c to G_R with crack growth. However, given its simplicity, and since no G_R characterization data is typically available, it is often used as a first-order conservative model. A more complex cohesive law such as tri-linear law may be used to represent the transition from G_c to G_R [15]. In this study, the effect of modeling this transition is investigated by comparing the results obtained when assuming a bi-linear law vs tri-linear at the tape/fabric interface. The tape/fabric interface was considered for this investigation because there is a marked difference between G_c and G_R for this interface and it was the first interface to delaminate.

The tri-linear law is defined as a sum of two bi-linear laws [14]. The properties used for the two bi-linear laws are given in Table 3. The penalty stiffness K_n is defined such that the displacement jump across the crack surfaces at peak stress is the same for both the bi-linear laws. The Benzeggagh and Kenane (BK) [10] exponent η is defined such that G_c matches the 50% mixed mode bend test data.

Table 3 Strength and Fracture Properties for Tri-linear Cohesive Law

	GI (N.mm^{-1})	GII (N.mm^{-1})	Y_T (Mpa)	K_n (MPa/mm)	η
Tape/Fabric I	0.294	1.228	80	50000	1.3
Tape/Fabric II	0.288	0.111	9	5625	5

The transverse interface normal strength (Y_T) is an experimentally determined property. However, this property has been observed to depend on the test used to measure it. Even when using the same test, it has been observed to be dependent on the volume of the specimen used. For the material used in this study, Y_T has been reported to vary between 80.1 and 127 MPa ([12],[16]). The effect of the full range of measured Y_T values on the solution was not studied since, given the difference between maximum and minimum value of Y_T, it would require further investigation to establish the adequate mesh size required to capture the cohesive response for the full range of Y_T values.

Three scenarios using different material properties, based on the experimental data available, and cohesive laws were studied and compared to test data as shown in Figure 9. The scenarios considered were:

A: Bi-linear cohesive law with damage onset (G_c) and low Y_T (80 MPa) for both intralaminar and interlaminar damage.

B: Bi-linear cohesive law with damage progression (G_R) and high Y_T (89 MPa) for both intralaminar and interlaminar damage.

C: Tri-linear cohesive law with damage progression (G_R) and hight Y_T (89MPa) for interlaminar damage along tape/fabric interface. Bi-linear cohesive law with damage onset (G_c) and high Y_T (89 MPa) for intralaminar and interlaminar damage in the tape.

Cases A and B aimed at bounding the numerical predictions by using minimum and maximum values for interlaminar/intralaminar strengths and toughnesses, based on the experimental data available. Case C is used to study the effect of modeling the transition between G_c to G_R with crack growth for tape/fabric interface, and whether that affects the predicted damage morphology and leads to better agreeement between predicted and measured load-displacement curves.

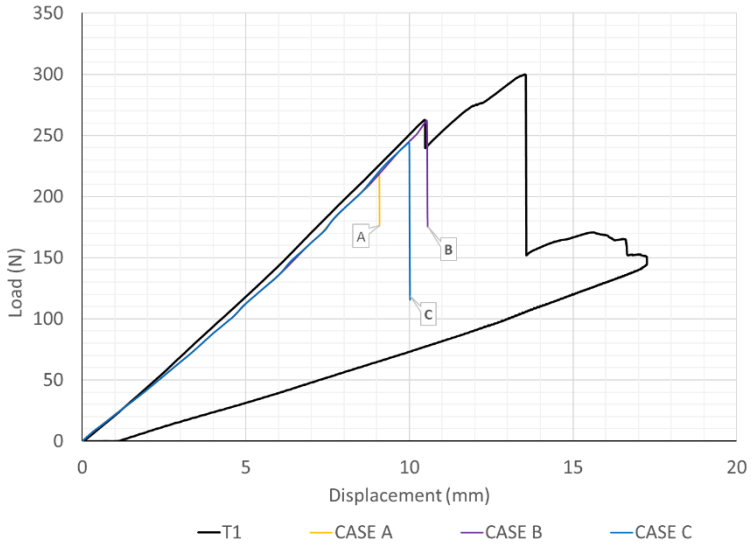

Figure 9. Effect of G_R, Gc, Y_T and Tri-linear Cohesive Law on Predicted Load versus Displacement Response.

Figure 9 shows that cases A and B straddle the tri-linear law results. However, the initial load drop observed in the test is not predicted by the tri-linear law. In addition, incorporating the tri-linear law did not contribute to capturing the subsequent re-loading observed experimentally.

The predicted damage at the skin/flange (tape/fabric) interface for the three cases at peak load is shown in Figure 10.

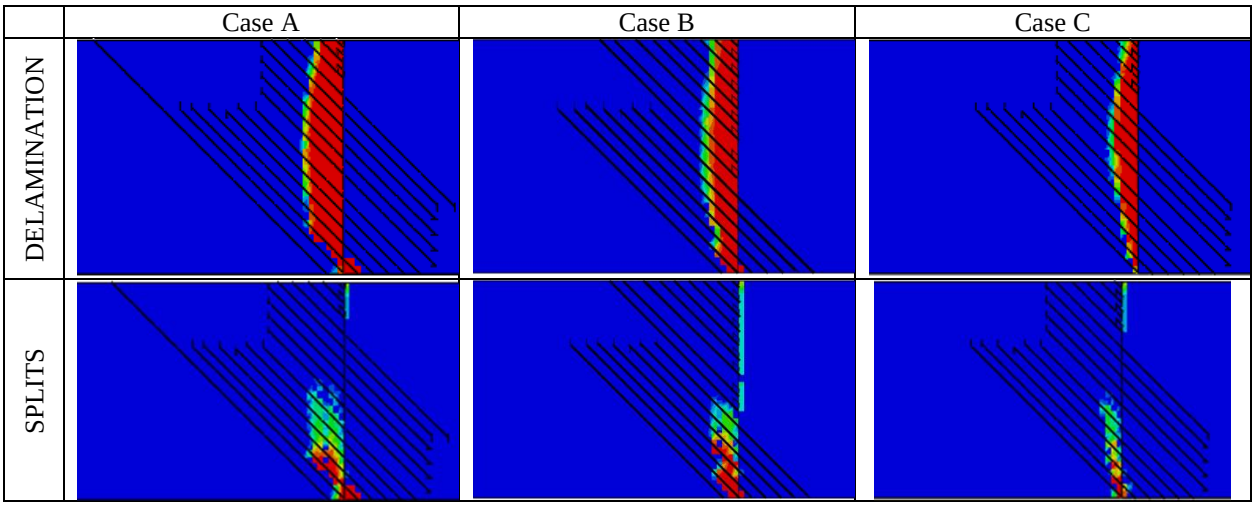

Figure 10. Damage Morphologies Compared for Cases A, B & C

Figure 10 indicates that in case A more damage is predicted at the tape/fabric interface than in the other two cases. This is due to the lower damage onset (G_c) used at the tape/fabric interface, which offers lower resistance to delamination compared to the G_R values used for cases B and C. The higher G_R value used in cases B and C prevents the delamination from growing as much along the tape/fabric interface and promotes migration to the lower interface via multiple matrix cracks. However, as mentioned previously, subsequent to the initial load drop, this migration does not lead to further resistance and eventual re-loading as observed in the experiments. This indicates that the quantitative effect on the load-displacement response of the complex damage progression is not yet being captured. This may be caused by the numerical model not being able to capture the apparent increase in toughness that may result from the complex damage interactions. Alternatively, it could also be due to a crack growth increment dependence of the tape fracture properties, both intralaminar and interlaminar, which is currently not accounted for due to a lack of characterization data. Further testing and characterization are ongoing to clarify this issue.

2. Effect of Thermal Residual Stresses

When the skin and flange are cocured there is a coefficient of thermal expansion mismatch between the epoxy resin and fibers within each ply and between plies. This results in thermal residual stresses. The effect of including the thermal residual stresses on the predicted load-displacement response, for a $\Delta T = -136^{o}C$, is shown in Figure 11.

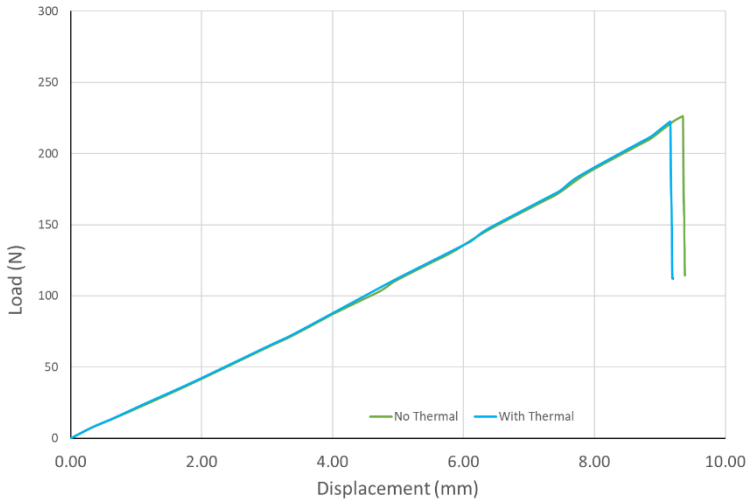

Figure 11. Effect of Thermal Residual Stresses

The thermal residual stresses decrease the peak load by about 3%. Thermal residual stresses appear to promote delamination in the tape/fabric interface and the 45° tape adjacent to the fabric (Figure 12a) while slightly suppressing damage in the remaining layers (Figure 12b).

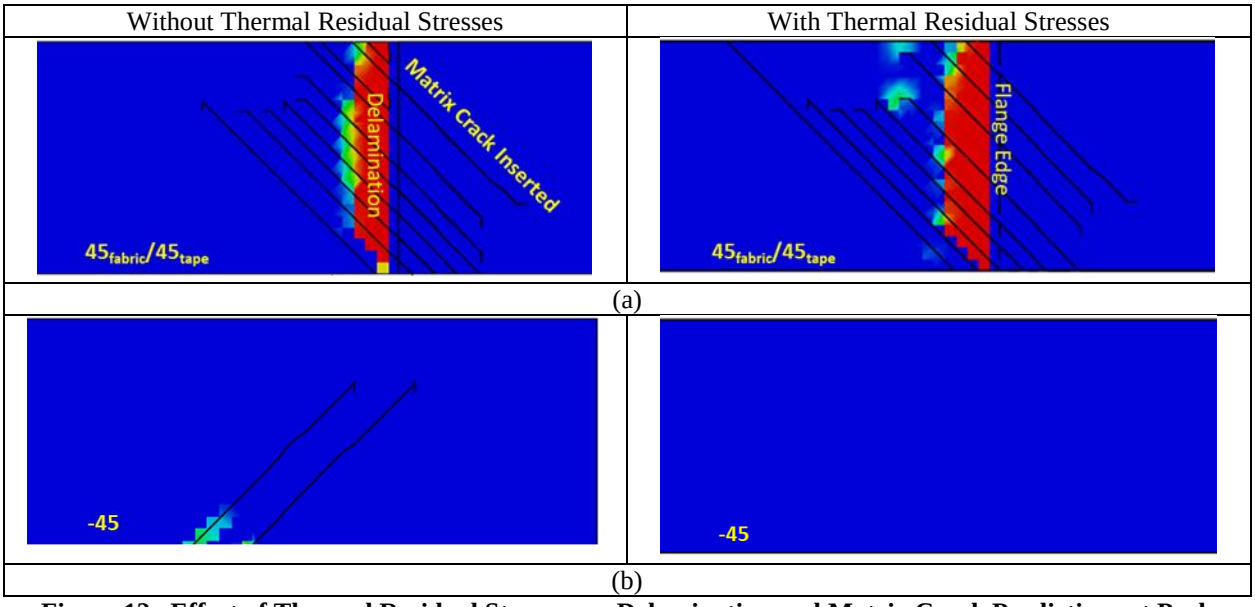

Figure 12. Effect of Thermal Residual Stresses on Delamination and Matrix Crack Predictions at Peak Load.

The suppression of damage in some plies due to thermal residual stresses combined with tri-linear cohesive law in the tape/fabric interface could provide some further resistance to damage migration. However, this is not addressed in this paper.

VI. Conclusions

A series of tests of a thin laminate with a flange loaded in a three-point bend configuration were performed. The specimen design and loading configuration was aimed at representing a skin-stringer debonding scenario. Preliminary results are reported and compared to the simulations preformed using the FNM-DCZE approach. Sensitivity of the simulations results to mesh refinement, intralaminar strength, critical energy release rate, and cohesive law chosen for the fabric/tape interface were studied.

Initial results show qualitatively a good correlation between the analysis and experiment. The simulations successfully capture multiple delamination migrations via matrix cracks in a sequence that resembles closely what was observed experimentally.

Quantitatively, while the first peak load seems well predicted, the subsequent re-loading observed in the experiments is not captured. To increase the fidelity of the model, a tri-linear law was applied to the tape/fabric interface. However, it did not improve the agreement between simulated and measured load-displacement curves after the first load peak. Thermal residual stresses, when included in the analysis, appear to aid damage progression in some plies while suppressing them in others, but overall did not affect significantly the load-displacement curve.

It is not clear whether the quantitative discrepancies observed after the first load peak are due predominantly to lack of fidelity of the numerical model in capturing damage mode interaction or to the limited tape characterization data, which currently encompasses only growth onset. Additional experimental work is ongoing to obtain characterization data that can help understand and address the causes for the observed quantitative discrepancy.

Acknowledgements

The authors would like to thank the National Aeronautics and Space Administration (NASA) for providing funding for this work under Contract Number: NNL09AA00A and 80LARC17C0004. Any opinions, findings, and conclusions or recommendations expressed in this material are those of the author(s) and do not necessarily reflect the views of the National Aeronautics and Space Administration.

References

[1] Selvarathinam, A., Rousseau, C.Q., Engelstad, and Flansburg, L. “Role of FEA, Closed-Form, and Empirical Models in Certifying Aircraft Composite Structures,” *AIAA SciTech*, 2016-1232.

[2] Wanthal, S., Schaefer, J., Justusson, B., Hyder, I., Engelstad, S., Rose, C.A. “Verification and Validation Process for Progressive Damage and Failure Analysis Methods in the NASA Advanced Composites Consortium,” 32nd American Society for Composites Annual Technical Conference, 2017.

[3] Saether, E. and Glaessgen, E. “The Development of Directional Decohesion Finite Elements for Multiscale Failure Analysis of Metallic Polycrystals,” NASA/TM-2009-215715, 2009.

[4] Chen, B.Y., Pinho, S.T, De Carvalho, N.V., Baiz, P.M. and Tay, T.E.. “A Floating Node Method for the Modelling of Discontinuities in Composites,” *Engineering Fracture Mechanics*, 27:104-134, 2014.

[5] Hillerborg, A., Modeer, M. and Peterson, P.E., “Analysis of Crack Formation and Crack Growth in Concrete by Means of Fracture Mechanics and Finite Elements,” *Cement and Concrete Research*; Vol. 6., 773-782, 1976.

[6] Seshadri, B.R., De Carvalho, N.V., Ratcliffe, J.G., Mabson, G.E., and Deobald, L.R., “Simulating the Clamped Tapered Beam Specimen under Quasi-Static and Fatigue Loading using Floating Node Method”, AIAA SciTech, 2018-0971.

[7] Greenhalgh, E.S., C. Rogers, and Robinson, P. “Fractographic observations on delamination growth and the subsequent migration through the laminate,” *Composites Science and Technology*, Volume 69, Issue 14, Pages 2345-2351, 2009.

[8] Czabaj, M.W., Davidson, B.D. and Ratcliffe, J.G. “A Modified Edge Crack Torsion Test for Measurement of Mode III Fracture Toughness of Laminated Tape Composites,” 31st ASC Technical Conference, Williamsburg, VA, USA, 2016.

[9] De Carvalho, N.V., Seshadri, B.R., Ratcliffe, J.G., Mabson, G.E., and Deobald, L.R., “Simulating Matrix Crack and Delamination Interaction in a Clamped Tapered Beam,”, 32nd ASC Technical Conference, West Lafayette, IN., 2017.

[10] Benzeggagh M.L., Kenane M. Measurement of mixed-mode delamination fracture toughness of unidirectional glass/epoxy composites with mixed-mode bending apparatus. Compos Sci Technol 1996;56(4):439–49.

[11] Turon, A., Camanho, P.P., Costa, J., and Renart, J. 2010. "Accurate simulation of delamination growth under mixed-mode loading using cohesive elements," Composite Structures 92, 1857-1864.

[12] The Boeing Company, “Advanced Composites Project for Certification Timeline Reduction,” NASA/CR-2016-NNL10AA05B.

[13] Pereira A.B., de Morais A.B., 2004. "Mode I Interlaminar Fracture of Carbon/Epoxy Multidirectional Laminates," *Compos Sci Technol*; 64(13-14):2261-2270.

[14] Dávila, C.G., Leone, F.A., Song, K., Ratcliffe, J.G., and Rose, C.A., "Material Characterization for the Analysis of Skin/Stiffener Separation," 32nd American Society for Composites Annual Technical Conference, 2017.

[15] Dávila C.G., Rose C.A., Camanho P.P., 2009. "A Procedure for Superposing Linear Cohesive Laws to Represent Multiple Damage Mechanisms in the Fracture of Composites," *Int J Fracture*; 158(2):211-223.

[16] O'Brien T.K., Chawan, A.D., Krueger, R., and Paris, I., "Transverse Tension Fatigue Life Characterization Through Flexure Testing of Composite Materials," NASA/TM-2001-211035.